CrystEngComm

HIGHLIGHT

View Article Online
View Journal | View Issue

Cite this: *CrystEngComm*, 2020, **22**, 1500

Vacancy-engineered catalysts for water electrolysis

Songa Choi, † Yeji Park, † Heesu Yang, † Haneul Jin, Gracita M. Tomboc and Kwangyeol Lee *

Received 27th November 2019,
Accepted 4th January 2020

DOI: 10.1039/c9ce01883b

rsc.li/crystengcomm

The development of electrochemical energy conversion and storage technologies is pivotal to the full-fledged utilization of renewable energy sources. The successful commercial application of water electrolysis to produce hydrogen gas, in particular, requires highly active electrocatalysts that can operate for prolonged periods. However, the high activity and high durability of electrocatalysts are often mutually exclusive. Recent studies have demonstrated that vacancy engineering might effectively modulate the electronic structures of catalysts, which can lead to high catalytic activity. Furthermore, it has been shown that vacancies are closely related to catalyst stability under operational conditions. To understand the benefits of vacancies in the catalyst structures, we discuss the recent advances in the development of vacancy-engineered catalysts for water electrolysis. In addition, we discuss the present limitations in this nascent field and provide directions for valuable future research.

1. Introduction

With the rapid consumption of fossil fuels and the associated serious environmental problems, the global demand for sustainable energy production from carbon-neutral fuels has increased continuously in the past decades. The production of hydrogen *via* electrochemical water splitting is considered one of the most promising energy sources due to the high energy density of hydrogen and the pollutant-free production process. However, the large operational potential window for the main water splitting reactions—hydrogen evolution reaction (HER) and oxygen evolution reaction (OER)—significantly hinders the commercialization of the water electrolysis system. Catalysts play a vital role in efficient energy conversions by decreasing the electrical energy usage during water electrolysis. Therefore, the development of active and durable catalytic materials for both HER and OER is an essential requirement for the advancement of water electrolysis technology.

Efficient catalysts require optimized surface physicochemical properties for facile adsorption and desorption of intermediates. Recently, vacancy engineering on the catalyst

Department of Chemistry and Research Institute for National Sciences, Korea University, Seoul 02841, Republic of Korea. E-mail: kylee1@korea.ac.kr
† These authors contributed equally to this work.

Haneul Jin

Dr. Haneul Jin (Front line), Heesu Yang, Songa Choi, Yeji Park, and Dr. Gracita M. Tomboc (back line: from left to right) are currently working in inorganic chemistry under the supervision of Prof. Kwangyeol Lee at the Department of Chemistry, Korea University (South Korea). H. Yang has been working on synthesis of nanoscale materials and their applications toward water splitting reaction. S. Choi is involved in designing noble metal-based functional nanomaterials for energy conversion/storage and CO_2 conversion. Y. Park is interested in the design of hetero-nanostructured catalysts and the development of functional nanomaterials for energy conversion. Dr. G. M. Tomboc is focused on advanced materials processing of ideal electrode materials for electrochemical energy storage system applications such as supercapacitor and water splitting process. Dr. H. Jin is interested in the development of synthetic methods for phase-controlled nano-catalysts and investigation of water splitting reaction mechanism on the heterogeneous catalyst surfaces.

surfaces has emerged as an effective strategy to enhance the HER and OER performances by controlling the surface electronic and atomic structures. The modification of the surface electronic structure adjusts the adsorption energy of the intermediates (*e.g.*, *H for HER; *OH, *OOH for OER) on the catalyst surface and promotes charge transfer at the interface between the electrolyte and the electrodes.[1,2] The coordination-unsaturated structure derived from vacancy engineering generates catalytically active sites for water electrolysis on the catalyst surface. However, the development of vacancy-engineered catalysts for electrochemical water splitting is only in its infancy.

In this review, we provide a brief overview of the vacancy engineering of electrocatalysts for water-splitting reactions, focusing on the nature of the vacant sites on the catalysts and their effect on the water-splitting reaction. First, we describe the three aspects of vacancy engineering that affect catalytic performances: (1) formation of low-coordination sites, (2) reaction kinetics control, and (3) modulation of electronic structures. Thereafter, we summarize the performance of vacancy-engineered catalysts in their applications toward HER and OER. Finally, we discuss the current limitations of vacancy-engineered catalysts and the future research directions for the development of high-performance vacancy-engineered catalysts for the electrochemical water-splitting process.

2. The effects of catalyst vacancies on electrochemical water splitting

The formation of the vacancies on an electrocatalyst can effectively modulate the local atomic structure, which creates a low-coordinated local geometry, and changes the electron configuration, thereby leading to an increase in the number of active sites, surface energy, and electron transfer, which are crucial for the efficient performance of catalysts in electrochemical water splitting.[3] Therefore, understanding the relationship between the vacancy and electrocatalytic performance is important for the rational design of a high-performance catalyst toward electrochemical HER and OER (Scheme 1). In this section, we discuss the beneficial effects of vacant sites on the electrocatalytic performance toward water splitting.

Kwangyeol Lee

Professor Kwangyeol Lee (born in 1971) obtained his Ph.D. degree (1997) in Chemistry from the University of Illinois at Urbana–Champaign. After fulfilling his military obligation, he joined Korea University in 2003 as a Chemistry faculty member, before being appointed professor. He is the recipient of the 2009 Wiley-KCS Young Scholar Award and 2019 Excellent Research Award (KCS Inorganic Chemistry Division). His current interests lie in the development of synthesis methods for nanoscale materials, applications of nanomaterials in biomedical fields, and development of nanotechnologies to support the environment by creating sustainable energy sources.

2.1. Formation of low-coordination sites

Low-coordinated sites serve as active sites on catalysts to promote catalytic reactions[4] owing to the high density of their dangling bonds, namely *coordinatively unsaturated sites* (CUSs), which are highly reactive. For instance, microkinetics mode-based density-functional theory (DFT) calculations demonstrated that low-coordinated gold atoms at the corners and edges of nanoparticles act as active sites in a CO oxidation reaction.[5] Similarly, vacant sites can lower the coordination number (CN) of the adjacent sites and modulate the local electronic structures. Sun *et al.* demonstrated that the ultrathin Co_3O_4 structure offers a considerably large fraction of coordinatively unsaturated surface atoms that serve as active sites to facilitate the OER.[6] As shown in Fig. 1A, the adsorption energy of H_2O molecules on Co^{3+} atoms was optimized by the gradual decrease in their CNs from 6 to 3, thereby indicating that a low CN could lead to high catalytic activity for the OER. For porous Co_3O_4 thin sheets, the presence of numerous pores decreased the CN of Co^{3+} atoms to 4 or even up to 3, and the thickness of half a unit cell enabled them to expose all the Co^{3+} atoms on their surfaces, thereby demonstrating that all the Co^{3+} atoms could function as active sites to catalyze the water oxidation reactions. Furthermore, the CUSs formed by S-vacancies on the edges of MoS_2 were demonstrated as active catalytic sites and were considered key descriptors to evaluate the catalytic activity of MoS_2-based materials.[7–9] When the S-vacancies are introduced, new bands appear in the gap near the Fermi level, thereby indicating that these states are localized around the S-vacancy (Fig. 1B). Additionally, the bands move closer to the Fermi level and increase the number of gap states with increasing S-vacancies (Fig. 1C), thereby leading to an increase in the active site density and improvement of the HER catalytic performance. Furthermore, the electronic structure of MoS_2 was highly dependent on the coordination of the Mo metal and its d-electrons. A semiconducting behavior and metallic conductivity can be observed when the non-bonding d-orbitals are fully and partially occupied, respectively.[10] In addition, the high exposure of the edges of MoS_2 nanosheets with unsaturated coordination and dangling bonds is crucial for their application in catalysis, electronics, and sensors, which require the involvement of a highly active surface.

Chen *et al.* designed a pseudo-cubic $SrCo_{0.9}Ir_{0.1}O_{3-\delta}$ perovskite that exhibits *in situ* formed vacancies during electrochemical cycling.[11] During the electrochemical treatment within the potential range of 1.0–1.7 V at a scan rate of 10 mV s^{-1} in 0.1 M $HClO_4$, Sr and Co were leached out, and a

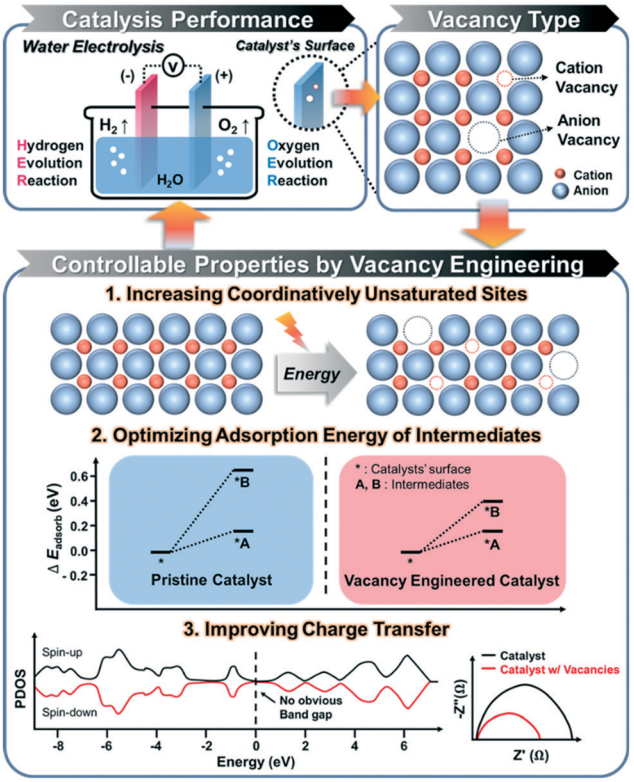

Scheme 1 Illustration of the strategies for enhancing the performance of electrocatalytic water splitting *via* vacancy engineering.

surface reconstruction occurred, as shown in Fig. 1D. Then, the $SrCo_{0.9}Ir_{0.1}O_{3-\delta}$ perovskites contained a higher number of oxygen vacancies in the lattice than in its initial pseudo-cubic structure. X-ray absorption spectroscopy (XAS) analysis revealed that compared to the case in IrO_2, the valence state of Ir in $SrCo_{0.9}Ir_{0.1}O_{3-\delta}$ slightly shifted toward >4+. Assuming that the valence state of Ir is 5+, the δ (oxygen non-stoichiometry) in $SrCo_{0.9}Ir_{0.1}O_{3-\delta}$ can reach a minimum value, which indicates that a high number of oxygen vacancies must exist in $SrCo_{0.9}Ir_{0.1}O_{3-\delta}$ and that both Co and Ir must be highly under-coordinated. To support this assumption, Fourier transformed (FT) extended X-ray absorption fine structure (EXAFS) spectra at the Ir L_{III}-edge were recorded to demonstrate that the Ir in $SrCo_{0.9}Ir_{0.1}O_{3-\delta}$ is highly under-coordinated with a CN of ~4.9 and that the under-coordinated IrO_x octahedron considerably improved the catalytic activity toward the OER.

2.2. Optimizing the adsorption energy of intermediates

Both HER and OER mechanisms consist of multi-step reactions such as adsorption, reduction/oxidation, and desorption processes;[12,13] their catalytic surfaces require suitable surface energies at each step.[14] Luo *et al.* showed that the vacancy-induced hydrogen binding energy optimization in mesoporous MoO_{3-x} could exhibit excellent HER activity under both acidic and alkaline conditions.[15] DFT calculation revealed that the oxygen vacancies close to Mo^{5+} served as electron acceptors and favored the adsorption of water molecules in alkaline media (or H_3O^+ in acidic media), which lowered the HER energy barrier. The HER process was facilitated by the cooperation between Mo^{5+} and oxygen vacancies that led to the promotion of H_2O adsorption and H–H bond formation on two adjacently adsorbed H_{ads} and H_2O_{ads} species, as shown in Fig. 2A. Under an alkaline condition, a fast charge-transfer process was the only effective method of obtaining OH^- during the reduction and formation of adsorbed H_2O_{ads} and H_{ads} species and the release of H_2. Additionally, Mo^{5+} ions donate electrons to become Mo^{6+} and then accept electrons to transform back to Mo^{5+}. Similarly, Cheng *et al.* demonstrated that 2D Cr_2CO_2, modified with a transition metal and with engineered carbon vacancy, could improve the HER performance.[16] The formation of carbon

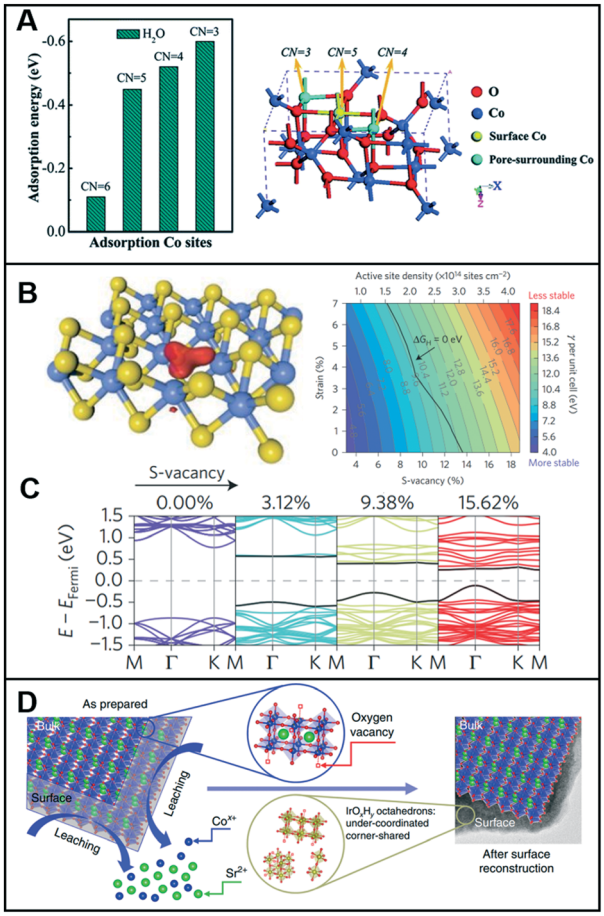

Fig. 1 (A) Calculated adsorption energy for the H_2O molecules on Co^{3+} sites with different CNs (left), and crystal structure showing the different CNs for surface and pore-surrounding Co^{3+} atoms. Reproduced with permission from ref. 6. Copyright 2014 Royal Society of Chemistry. (B) Kohn–Sham orbitals (red) are localized around the S-vacancies in MoS_2 (left) and colored contour plot of surface energy per unit cell γ (with respect to the bulk MoS_2) as a function of the S-vacancy and uniaxial strain (right). Color bar represents the value of γ. (C) Band structure with increasing S-vacancy concentrations (calculated using the full 4 × 4 unit cell). Reproduced with permission from ref. 9. Copyright 2016 Nature Publishing Group. (D) Schematic illustrating the surface reconstruction over the $SrCo_{0.9}Ir_{0.1}O_{3-\delta}$ surface. Reproduced with permission from ref. 11. Copyright 2019 Nature Publishing Group.

vacancies (V_C) in 2D Cr_2CO_2 can be a natural phenomenon because the calculated formation energy of V_C decreased as the percentage of V_C increased. Additionally, when the concentration of V_C reached up to 25%, the ΔG_{H^*} of V_C-Cr_2CO_2 was very close to the ΔG_{H^*} value obtained for the perfect $CrCO_2$. This suggests that V_C-Cr_2CO_2 could provide an optimal reaction kinetics toward HER.

On the contrary, it is imperative to control the reaction kinetics for the OER because of the multi-electrons ($4e^-$) participating in this process.[14,17,18] The rate-determining step (RDS) of the OER may vary depending on the O-adsorption/desorption on the catalyst surface. This implies that the formation of OOH is the RDS on a weak O-adsorbate and *vice versa*.[12,19] Thus, the optimization of the bond strength between the intermediates and catalyst is crucial to facilitate the OER process. Additionally, the nucleophilic attack of adsorbed oxygen by water/hydroxide has been proposed to describe the mechanism of O–O bond formation during the OER. Pfeifer *et al.* revealed that the electrophilic oxygen species adsorbed on the surface and in the subsurface of amorphous Ir were indispensable for the high activity of hydrated amorphous $Ir^{III/IV}$ oxyhydroxide (IrO_x), compared to crystalline IrO_2.[20] During the CO oxidation, they determined which oxygen atom in IrO_x (O^{I-} or O^{II-}) may serve as the active species for the OER. They found that bulk O^{I-} species are more electrophilic than their bulk O^{II-} counterparts, as they were weakly bound to IrO_x. The reactivity of the O^{I-} species was suspected to play a critical role in the OER when reacted with OH/H_2O to form the OOH intermediate because the electrophilic O^{I-} species in amorphous $Ir^{III/IV}$ oxyhydroxide could be susceptible to nucleophilic attacks. In line with this, Nong *et al.* reported that Ni leaching during catalyst activation at high potential could lead to the formation of Ir lattice vacancies and numerous d-band holes in the formed IrO_x shell in IrNi alloy nanoparticles.[21] The oxygen ligands adjacent to the lattice vacancies were suggested to possess an electrophilic character that initiates the formation of O–O bonds and weakens the kinetic barrier during the OER, eventually resulting in high activity.

Meanwhile, Lee *et al.* investigated the transition metal (TM) vacancies (V_M) formed during the simultaneous incorporation of Ni and Fe metals into the same crystal structure.[22] The different preferential oxidation states (2+ for Ni and 3+ for Fe) would cause the V_M to achieve charge neutrality with oxygen; the addition of Fe^{3+} into a NiO matrix resulted in the formation of NiFe-V_M-O. As shown in Fig. 2B, this vacancy formation altered the bond strengths of adjacent Ni–O and Ni–TM, which improved the catalytic activity of the modified catalyst as compared to its original state, NiO. In terms of electronic structure modification of the active site, the energy of O-adsorption in NiFe-V_M-O was lower than that in NiO owing to its flexible geometric distortions that can accommodate adsorbates easily.

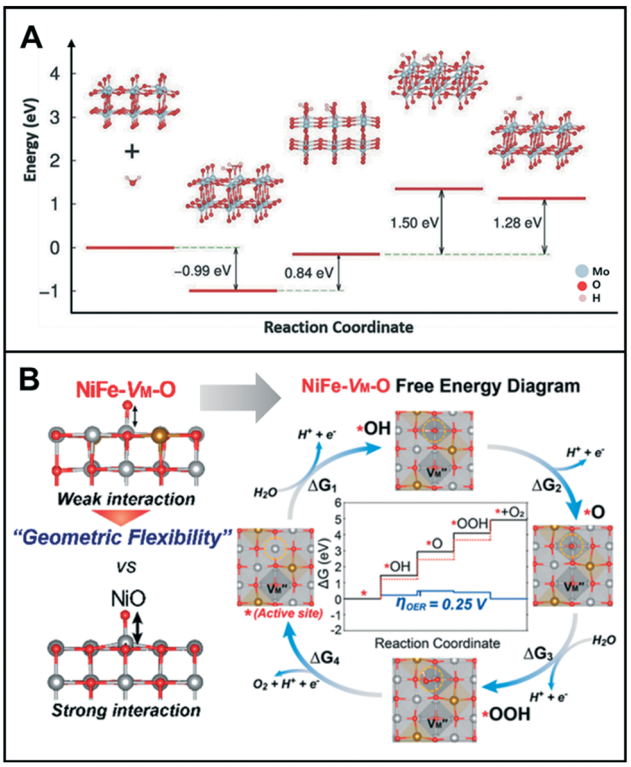

Fig. 2 (A) Proposed reaction pathway, and the energy barrier profiles of mesoporous MoO_{3-x} in 0.1 M KOH. Reproduced with permission from ref. 15. Copyright 2016 Wiley-VCH. (B) Free energy diagrams of NiFe-V_M-O at 0 V (black line) and 1.23 V (blue line). Red dashed lines correspond to the free energies of the ideal catalyst with 0 V overpotential. Top views of each reaction step are presented. Each color indicates Ni (gray), Fe (brass yellow), and O (red). Reproduced with permission from ref. 22. Copyright 2019 American Chemical Society.

2.3. Improving charge transfer

Most metal oxides have lower electrical conductivity than metals, resulting in lower electrochemical efficiency. Oxygen vacancy-engineered catalysts have been suggested to overcome the low electrical conductivity problem of transition metal oxides.[23–25] Wang *et al.* reported that reduced mesoporous Co_3O_4 nanowires (NWs) with abundant oxygen vacancies have lower charge-transfer resistance than the pristine Co_3O_4 NWs.[26] The total density of states (TDOSs) and the projected DOSs (PDOSs) calculation showed that the oxygen vacancies in Co_3O_4 NWs induced new defect states within the bandgap (Fig. 3A). The electron occupancy of the gap state was classified into three different states of occupied electrons, namely empty, occupied by one electron, or by two electrons, denoted as V_O^{2+}, V_O^{+}, V_O, respectively. According to the calculated formation energy (Fig. 3B), V_O^{2+} has the lowest formation energy for all the values of the Fermi level in the bandgap, indicating that the oxygen vacancy is most likely formed as V_O^{2+}. When the two electrons are excited, the formation energy of V_O^{2+} is about 1 eV. These calculated values suggested that the reduced Co_3O_4 NWs can easily produce the oxygen vacancies with two positive charges (V_O^{2+}), and the two electrons are delocalized near the oxygen vacancy and are easily excited into the conduction band, thus leading to enhanced electrocatalytic performance. Likewise, other metal

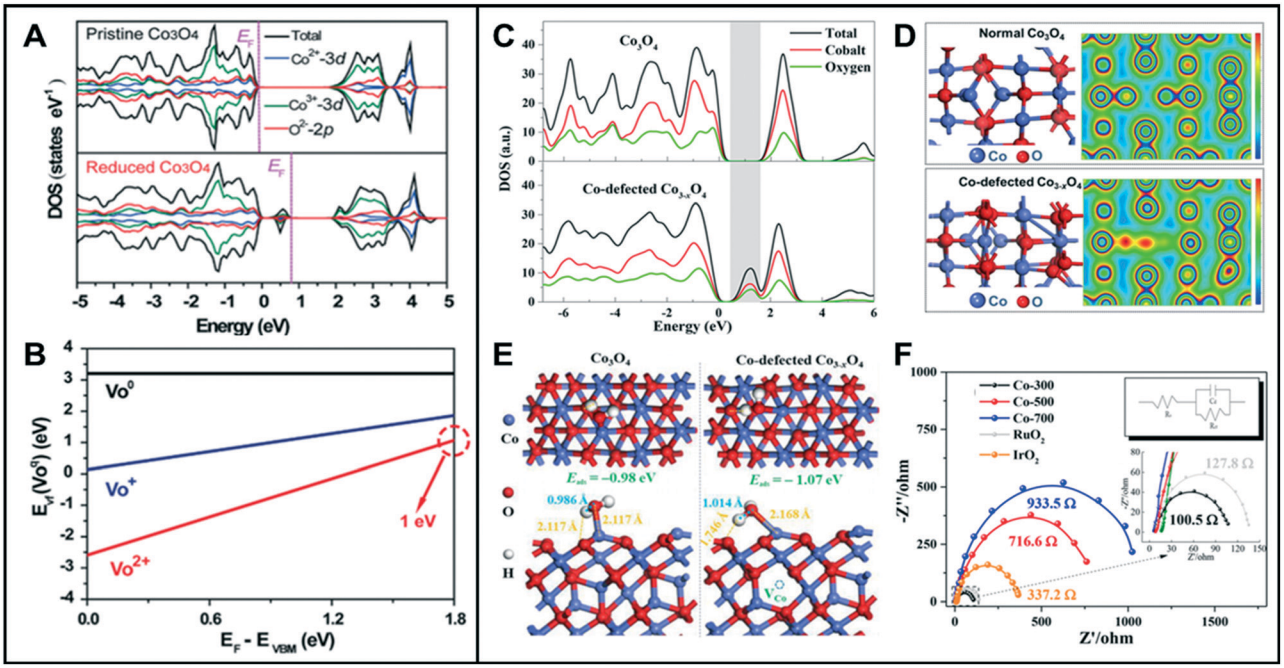

Fig. 3 (A) TDOS and PDOS of pristine Co_3O_4 and reduced Co_3O_4 with oxygen vacancies. (B) Calculated formation energies for the reduced Co_3O_4. V_O^{2+}, V_O^{+}, and V_O, denote that the gap state is empty, occupied by one electron, and occupied by two electrons, respectively. Reproduced with permission from ref. 26. Copyright 2014 Wiley-VCH. (C) TDOS and PDOS for Co_3O_4 and Co-defected $Co_{3-x}O_4$. (D) Optimized cell structures and the corresponding charge density mapping of normal Co_3O_4 and Co-defected $Co_{3-x}O_4$. (E) Optimized structures of water adsorbed at Co on the (111) surface (top and side views) of Co_3O_4 (left) and $Co_{3-x}O_4$ (right). (F) Electrochemical impedance spectroscopy (EIS) (inset: EIS fitting model; electrolyte resistance R_S, charge-transfer resistance R_{ct}, capacitive reactance C_d). Reproduced with permission from ref. 3. Copyright 2018 American Chemical Society.

oxides such as NiO nanorods (NRs) also showed great HER activities owing to the vacancy-induced electronic structural modification.[1] Zhao *et al.* reported the synthesis of ultrathin NiFe-layered double hydroxide (NiFe LDH-UF) nanosheets containing multi-vacancies, such as metal and oxygen vacancies, which enhanced their electronic conduction and HER reaction kinetics.[27] DFT calculations revealed the effect of multi-vacancies (V_O, V_{Ni}, and V_{Fe}) on the electronic structure of the NiFe LDH ultrafine nanosheets. While the monolayer and multi-layered LDH had noticeable band gaps, their calculated DOSs showed that there is no noticeable band gap around the Fermi level in the LDH-UF. This demonstrates the semi-metal-like character of the modified material, which can result in the enhancement of the electrical conductivity. Additionally, LDH-UF showed a lower charge-transfer resistance during electrochemical tests, compared with the LDH-bulk and LDH-monolayer, supporting the claimed excellent electrical conductivity.

Similar to anion vacancies, cation vacancies can promote the charge transfer by modifying the electronic structures of the catalysts. Zhang *et al.* demonstrated that Co deficient $Co_{3-x}O_4$, with structural distortion and electronic delocalization, enhanced the rate of carrier transport to participate in OER.[3] As the Co vacancies in Co_3O_4 are formed, the DOS for the occupied states from *ca.* 0.50 eV above the Fermi level increased and then showed a very small energy gap (Fig. 3C). The electronic structures of $Co_{3-x}O_4$ showed a considerable charge depletion, with more overlap areas of the electron wavefunction with neighboring O atoms compared to those of the pristine Co_3O_4 (Fig. 3D). The charge density of $Co_{3-x}O_4$ increased around the conduction band edge to form a more dispersive electronic structure than that of pristine Co_3O_4, which resulted in a fast carrier transport for the OER. Moreover, the deformation charge densities of adsorbed H_2O on Co_3O_4 and $Co_{3-x}O_4$ revealed that the Co-defective surface is more beneficial for the adsorption and desorption of water. When H_2O molecules were adsorbed onto the surface of the $Co_{3-x}O_4$ catalyst, one H atom from the adsorbed water of $Co_{3-x}O_4$ showed relatively strong interaction with O_s (surface O of $Co_{3-x}O_4$), which resulted in the extension of the H–OH bond length of the adsorbed water to 1.014 Å, compared to 0.986 Å for normal Co_3O_4. This result indicated that the Co-defective structure has the ability to facilitate the adsorption/desorption of intermediates and to improve the electronic conductivity, thus being highly favorable toward water splitting (Fig. 3E and F).

3. Classification of vacancy-engineered nanostructures and their catalytic performances in HER and OER

3.1. Anion vacancy

Among various forms of vacancies, anion vacancies are the most commonly used to improve catalytic performance

because they are easily formed and can often generate an ideal Fermi level for water splitting reaction.[9,26,28,29]

Oxygen evolution reaction. The oxygen vacancies in the metal oxides that have been intensively investigated as catalysts for the OER alter the physicochemical properties of materials such as atomic and electronic structures.

As mentioned in a previous section, low-coordination metal atoms are identified as the active sites of metal-oxide catalysts for water-splitting reaction.[30] Bao *et al.* synthesized oxygen-vacancy-rich NiCo nanosheets (NiCo-r) and compared the results with bulk NiCo and oxygen-vacancy-poor NiCo nanosheets (NiCo-p).[28] The O 1s X-ray photoelectron spectroscopy (XPS) spectra of the three materials exhibited a peak at 531.2 eV, with NiCo-r showing the highest intensity, which may be correlated to its low oxygen coordination and the high number of oxygen vacancies present compared to those in the others (Fig. 4A). The NiCo-r nanosheets showed enhanced activity toward the OER (320 mV at 10 mA cm^{-2}) than oxygen-vacancy-poor or bulk catalysts. This result was consistent with DFT calculation, which revealed that $NiCo_2O_4$ with oxygen vacancies has lower adsorption energy for H_2O (−0.75 eV) compared to the perfect surface (−0.41 eV) (Fig. 4B).

Asnavandi *et al.* reported that the NiFe (oxy)hydroxides with surface oxygen vacancies achieve enhanced OER performance.[31] X-ray absorption near edge structure (XANES) spectra displayed the relatively low oxidation states of Ni and Fe in NiFe–OOH, which may be associated with the presence of oxygen vacancies. Furthermore, to gauge the oxygen vacancy density, they fitted O 1s XPS spectra, which contains information of (1) lattice oxygen (530.1 eV), (2) oxygen loss in the material (531.7 eV), and (3) adsorbed oxygen throughout the surface (533.2 eV). The density of oxygen vacancy can be quantified roughly by the ratio of (2) to (1), and the density of NiFe with oxygen vacancies was 7.0, which is twice as high as that of the pristine one (3.2). NiFe with numerous vacancies exhibited enhanced OER current density (240 mA cm^{-2}) at an overpotential of 270 mV from pristine NiFe (100 mA cm^{-2}).

Ling *et al.* synthesized single-crystal cobalt oxide nanorods with exposed vacancy-rich pyramidal nano-facets.[32] The O-vacancy formation was identified by the O 1s XPS spectra of single-crystal (SC) CoO nanorods (NRs) (Fig. 4C). The peak at the middle binding energy (II) at 531.5 eV was attributed to the oxygen vacant sites with relatively low oxygen coordination. The large area of peak II revealed that the SC CoO NRs contain numerous O-vacancies on the surface. Moreover, the peak at ~536.0 eV of the O–K edge XANES spectra was associated with O deficiency, resulting in the presence of abundant O-vacancies on the surface of SC CoO NRs (Fig. 4D). This 1D SC CoO NRs exhibited an overpotential of 0.33 V (*vs.* RHE) in the OER. They explained that the conductivity of the metal oxides was further improved by creating O-vacancies on {111} facet and increasing the carrier concentration. Projected

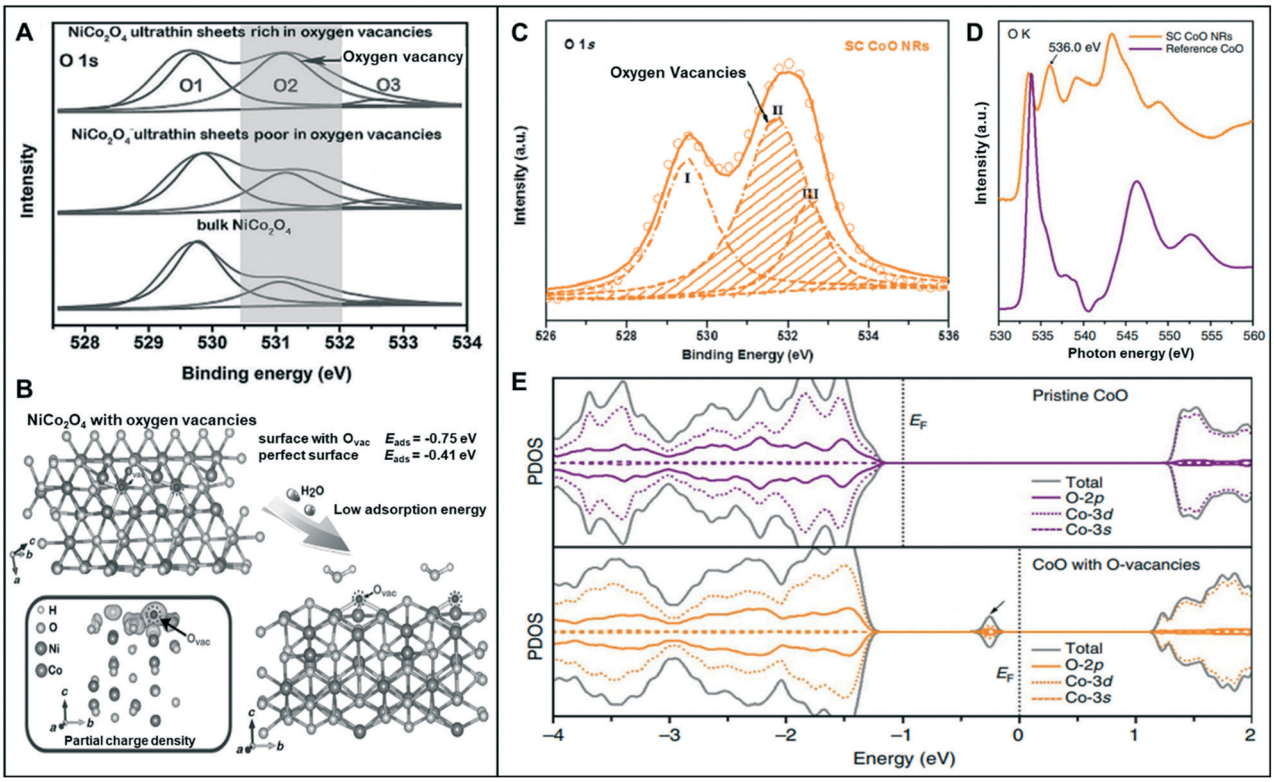

Fig. 4 (A) The O 1s XPS spectra of the $NiCo_2O_4$ nanosheets. (B) Schematic illustration of the adsorption of H_2O molecules onto the $NiCo_2O_4$ structure and the partial charge density of $NiCo_2O_4$ with oxygen vacancies. Reproduced with permission from ref. 28. Copyright 2015 Wiley-VCH. (C) O 1s XPS spectra of SC CoO NRs. (D) O–K edge XANES spectra of SC CoO NRs and reference CoO. (E) The projected density of states (PDOSs) on pristine CoO and CoO with O-vacancies. Reproduced with permission from ref. 32. Copyright 2016 Nature Publishing Group.

density of states (PDOS) on pristine CoO and CoO with O-vacancies was determined to examine the electronic structure, which correlated the formed O-vacancies in the bandgap of CoO to the observed strong adsorption of intermediates on the vacant sites and high electronic conductivity (Fig. 4E).

Hydrogen evolution reaction. In addition to the beneficial role of oxygen vacancy in the OER, a recent study on sulfur vacancies revealed the significance of S-vacancies in the enhancement of the HER performance. Lu *et al.* created sulfur vacancies on molybdenum sulfide ($MoS_{1.7}$) using hydrogen plasma, and obtained an overpotential of 143 mV at −10 mA cm^{-2} under acidic condition, which is lower compared to that of untreated catalysts ($MoS_{3.1}$, 206 mV) (Fig. 5A).[33] They explained that the enhancement of the HER activity was due to an increased active site density. The S 2p XPS spectra displayed peaks at binding energies (B.Es) of 163.5 eV and 162.3 eV, assigned to S^{2-}, and B.Es of 164.6 eV and 163.4 eV indexed to S_2^{2-} (Fig. 5B). While the peak intensities of Mo, including Mo^{IV} species (B.E at 232.6 eV for Mo $3d_{3/2}$ and B.E at 229.5 eV for Mo $3d_{5/2}$) did not show any changes, the normalized intensities of S^{2-} and S_2^{2-} in S 2p spectra showed a considerable decrease, which may be due to the numerous sulfur vacancies induced in the material. To evaluate the catalytic properties of the modified material, the group designed several models by changing the number of the sulfur vacancies on the MoS_2 lattice (4 × 4) and carried out a first-principles calculation (Fig. 5C). MoS_2 and MoS without defect sites have relatively large ΔG values (2.06 eV and ~−0.6 eV), which were reduced to almost 0 eV upon the formation of defect sites. However, an increase in the number of defect sites led to larger ΔG; thus, the catalytic activity was further improved by controlling the number of defect sites.

The placement of strain in the catalyst structure has been effective in optimizing the adsorption energy of the catalytic surface.[34] Li *et al.* combined the sulfur vacancy with strain effect to optimize the basal plane of monolayer 2H–MoS_2 (Fig. 5D).[9] Catalysts with various amount of vacancies (0.00–25.00%) were analyzed by DFT calculations to understand the HER activity dependence on the vacancy (Fig. 5E). The calculation results verified that the free energy (ΔG_H) related to hydrogen adsorption varied depending on the number of removed sulfur atoms. The free energy of pure 2H–MoS_2 was about 2 eV, but it reduced to almost 0 eV at 12.50% of sulfur vacancy. Li *et al.* concluded that ΔG_H might be reduced to 0 eV by applying the appropriate amount of strain in each case. The HER activity was measured with respect to the sulfur vacancy and strain-control in the catalyst (Fig. 5F). The modified catalyst with 12.5% S-vacancies and 1.35 ± 0.15% strain exhibited an overpotential of 170 mV at −10 mA cm^{-2} in HER, which was smaller than that of the catalyst modified with only S-vacancy (250 mV at −10 mA cm^{-2}) or with only strain.

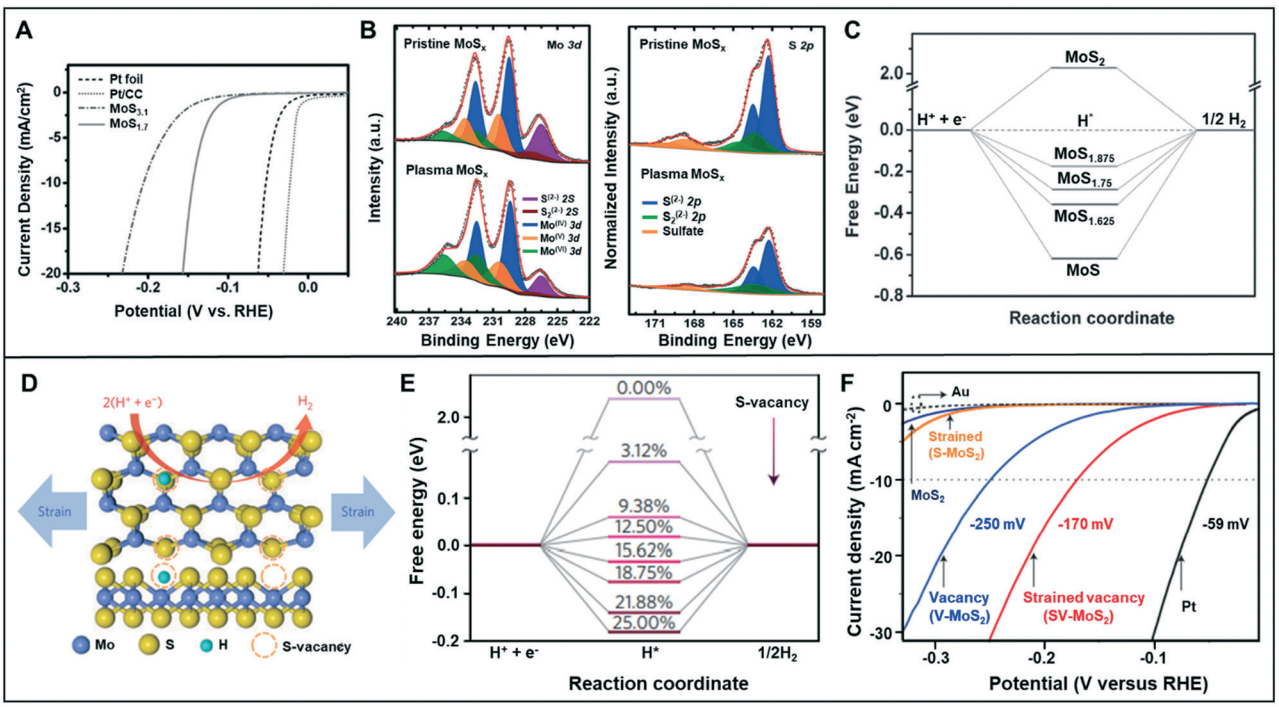

Fig. 5 (A) HER polarization curves for Pt foil, Pt/CC, $MoS_{3.1}$, and $MoS_{1.7}$ in 0.5 M H_2SO_4 solution. (B) The Mo 3d and S 2p XPS spectra of the pristine MoS_x and plasma MoS_x. (C) The free energy with different defective levels of MoS_2. Reproduced with permission from ref. 33. Copyright 2016 Wiley-VCH. (D) Schematic of the top (upper panel) and side (lower panel) views of MoS_2 with strained S-vacancies on the basal plane. (E) Free energy *versus* the reaction coordinate of HER for the S-vacancy range of 0–25%. (F) LSV curves for Au substrate, Pt electrode, as-transferred MoS_2 (strain: 0% and S-vacancy: 0%), strained MoS_2 without S-vacancies (S-MoS_2, strain: 1.35 ± 0.15% and S-vacancy: 0%), unstrained MoS_2 with S-vacancies (*V*-MoS_2, strain: 0% and S-vacancy: 12.5 ± 2.5%), and strained MoS_2 with S-vacancies (SV-MoS_2, strain: 1.35 ± 0.15% and S-vacancy: 12.5 ± 2.5%). Reproduced with permission from ref. 9. Copyright 2016 Nature Publishing Group.

3.2. Cation vacancy

Oxygen evolution reaction. To enhance the OER catalytic activity, Suntivich *et al.* suggested the importance of catalysts with cation e_g occupancy close to unity.[35] Cubic $CoSe_2$ with an optimal e_g filling showed great potential as an excellent catalyst. However, owing to its limited active sites, it exhibits unsatisfactory catalytic activity. Liu *et al.* introduced Co vacancy (V_{Co}) to modify the structure of $CoSe_2$ nanosheets with the aim of improving the OER activity (Fig. 6A).[36] The XPS spectra demonstrated the evident existence of the Co 2p satellite peak, which correlated to the antibonding orbital of Co and Se, and thus, the presence of V_{Co} (Fig. 6B). Additionally, X-ray absorption fine structure (XAFS) and its corresponding FT $k^3[\chi(k)]$ functions in R space detected a significantly different atomic sequence between the modified and bulk catalysts. As compared to the bulk catalyst (2.12 Å), the ultrathin $CoSe_2$ nanosheet showed a smaller R (Co–Se coordination value, 2.08 Å) and lower intensity peak. These changes were correlated to the reduced length of the bond between Co and Se, and the lowered CN, respectively. Through DFT calculations (Fig. 6C), adsorption energies of −0.63 eV and −0.85 eV were calculated for Co and V_{Co}, respectively, which were larger than that of the bulk catalyst with an adsorption energy of −0.38 eV. Ultrathin $CoSe_2$ nanosheets with numerous V_{Co}, which acted as active sites, exhibited a low overpotential of 0.32 V at 10 mA cm^{-2} for the OER.

Hydrogen evolution reaction. Kwong *et al.* reported an enhanced HER activity using the Fe-vacancy-rich FeP (Vc-FeP) nanoparticulate film that was prepared by leaching out Mg dopant.[37] DFT calculation revealed that the material has an ideal hydrogen adsorption energy of 0.02 eV (Fig. 6D). The HER activity of Vc-FeP exhibited improvement under both alkaline and acidic conditions, compared to pristine FeP or FeP replaced by Mg (Mg–FeP) (Fig. 6E), with overpotentials of 108 and 65 mV at −10 mA cm^2, respectively; it showed great stability even after 1 day in 1 M KOH, and 7 days in 0.5 M H_2SO_4 (Fig. 6F). The X-ray diffraction (XRD) analysis displayed a broadened peak width and reduced lattice spacings (Fig. 6G), with respect to the FeP film, which were correlated to the successful formation of Fe vacant sites.[38]

Likewise, Liu *et al.* utilized the appropriate hydrogen adsorption energy of the cation vacancies in five-fold twinned PtPdRuTe anisotropic structures (v-$Pd_3Pt_{29}Ru_{62}Te_6$ AS).[39] The v-$Pd_3Pt_{29}Ru_{62}Te_6$ AS exhibited a low overpotential of 39 mV in 0.5 M H_2SO_4 and 22 mV in 1.0 M KOH to achieve current densities of −10 mA cm^{-2}. They demonstrated that the activity of v-$Pd_3Pt_{29}Ru_{62}Te_6$ AS results from rapid charge transport and a substantial amount of exposed surface area of the anisotropic structure. The catalysts were stable for 30 h with a current density of −10 mA cm^{-2}.

3.3. Multi-vacancies

A combination of the anion and cation vacancies often produces synergy for the enhanced electrochemical activity for water-splitting reaction.

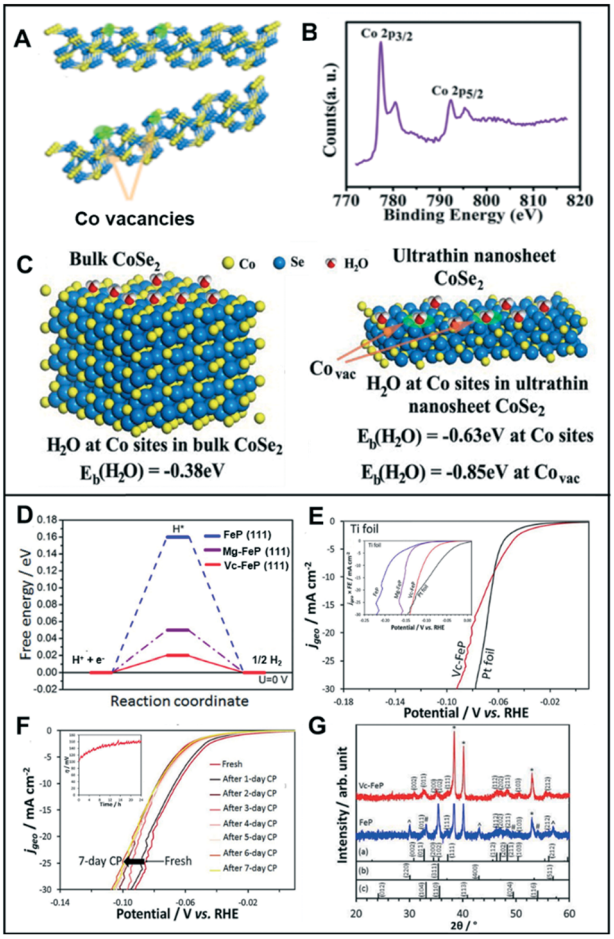

Fig. 6 (A) Schematic illustration of the formation of Co vacancies in $CoSe_2$ ultrathin nanosheets. (B) The XPS Co 2p of $CoSe_2$ ultrathin nanosheets. (C) Geometries and binding energies of H_2O molecules on Co sites and vacancies for bulk $CoSe_2$ (left) and ultrathin nanosheet $CoSe_2$ (right). Reproduced with permission from ref. 36. Copyright 2014 American Chemical Society. (D) Free energy diagram of FeP, Mg-FeP, and Vc-FeP (111) surfaces. (E) Polarization curves for the HER activity of Vc-FeP in 0.5 M H_2SO_4 (inset: HER activity in 1 M KOH). (F) The CP tests of Vc-FeP in 0.5 M H_2SO_4 (inset: stability test on Vc-FeP performed in 1 M KOH). (G) XRD data for FeP and Vc-FeP. The reference patterns of (a) orthorhombic FeP, (b) γ-Fe_2O_3, and (c) α-Fe_2O_3 also are shown. Reproduced with permission from ref. 37. Copyright 2017 Wiley-VCH.

Oxygen evolution reaction. Zhou *et al.* generated multiple types of vacancies of Co, Fe, and O (Fig. 7A).[40] The variation in the electronic structures of CoFe layered double hydroxides (LDHs) and modified-CoFe LDHs *via* chemical etching (E-CoFe LDHs) was characterized by XAFS, wherein obvious peak intensity changes were shown. Extended XANES oscillation functions revealed that the coordination environment of the metal atoms in the E-CoFe LDHs varied in favor of the electrochemical activity. A modified catalyst with multiple vacancies delivered a lower overpotential of 300 mV at 10 mA cm^{-2} compared to that delivered by pristine CoFe LDHs (Fig. 7B). Additionally, the fitted Nyquist plot of E-CoFe LDH catalyst demonstrated a smaller charge-transfer resistance for water oxidation as compared to the pristine one (Fig. 7C).

Similarly, Wang *et al.* proved that the CoFe LDH nanosheets with multiple types of vacancies could promote the intrinsic activity in the OER.[41] Furthermore, the ultrathin LDH nanosheets through Ar plasma etching (CoFe LDHs-Ar) resulted in the formation of multiple vacancies, including O, Co, and Fe vacancies. While the presence of oxygen vacancies facilitates the adsorption of intermediates such as OH*, O*, and OOH*, cationic vacancies cause the effective distributions of electrons and orbitals by adjusting the atomic environment of Co. With a potential increase in the valence state from Co^{2+} to Co^{3+}, Co^{3+} with the higher valence state has a low coordination, resulting in increased catalytic activity. CoFe LDHs-Ar with multiple vacancies showed low overpotentials of 266 mV at 10 mA cm^{-2} and 313 mV at a relatively high current density of 50 mA cm^{-2} compared to that of CoFe LDHs (321 mV and 409 mV, respectively).

Hydrogen evolution reaction. Yuan *et al.* introduced O and metal vacancies to LDH materials *via* the calcination process (Fig. 7D).[42] XRD data showed that the vacancy-containing NiFe LDH (v-NiFe LDH) has a noticeable broad peak, thus confirming the defect structure. The pair distribution function peaks associated with M–O and M–M were 2.05 and 3.10 Å, respectively. They both displayed lowered peaks in v-NiFe LDH, which indicate that O and M vacancies were formed. Furthermore, the bandgap energy of v-NiFe version was calculated as 2.16 eV, which is lower than that of the pristine version (2.85 eV). The presence of vacancies in v-NiFe LDH lowered the CN of Ni–OOH, which helped decrease the overpotential from 246 mV to 87 mV at −10 mA cm^{-2} (Fig. 7E). The fitted Nyquist plots showed that the charge-transfer resistance (R_{ct}) of v-NiFe LDH (3.17 Ω) was lower than that of the pristine NiFe LDH (6.99 Ω) (Fig. 7F), which may be related to the improved electroconductivity.

The electrocatalytic OER and HER performances of various catalysts and their vacancy types are described in Table 1. In addition, Fig. 8 summarizes the performance of recently reported vacancy-engineered electrocatalysts. The overpotentials are plotted against the types of vacancies to provide a visual illustration for the effective vacancy types toward the water-splitting reaction.

In general, the vacancies are classified into three types, namely anion vacancies, cation vacancies, and multi-vacancies. Anion vacancies are more easily formed, and oxygen vacancies are commonly observed with formed oxide-based electrocatalysts for both the OER and HER. In contrast, the formation of the cation vacancy is considerably challenging due to the high formation energy required, compared to the case with the anion vacancy.[39] As compared to the electrocatalysts without vacancies, the cation vacancy-engineered electrocatalysts remarkably lowered the overpotentials, and thus showed improved activity toward the OER and HER, as shown in Fig. 8, owing to their diverse chemical states that are conducive for the optimization of intermediate B.Es For the HER, the cation vacancy-controlled catalysts performed much better than the anion vacancy-engineered catalysts, with ~50 mV lower overpotentials.

Multi-vacancies with both cation and anion vacancies showed the synergistic effects of cation and anion vacancies toward enhancing the performances of the electrocatalysts. The presence of anion vacancies can effectively modulate the electronic structures, tune the adsorption energies of intermediates, and improve the electrical conductivity.[41] The presence of cation/metal vacancies can increase the valence state of nearby metal centers, which can also improve the reaction kinetics due to the increased surface area with a low CN of the catalytic active sites.[42] However, the examples for multi-vacancies are very limited, thus calling for a great synthetic

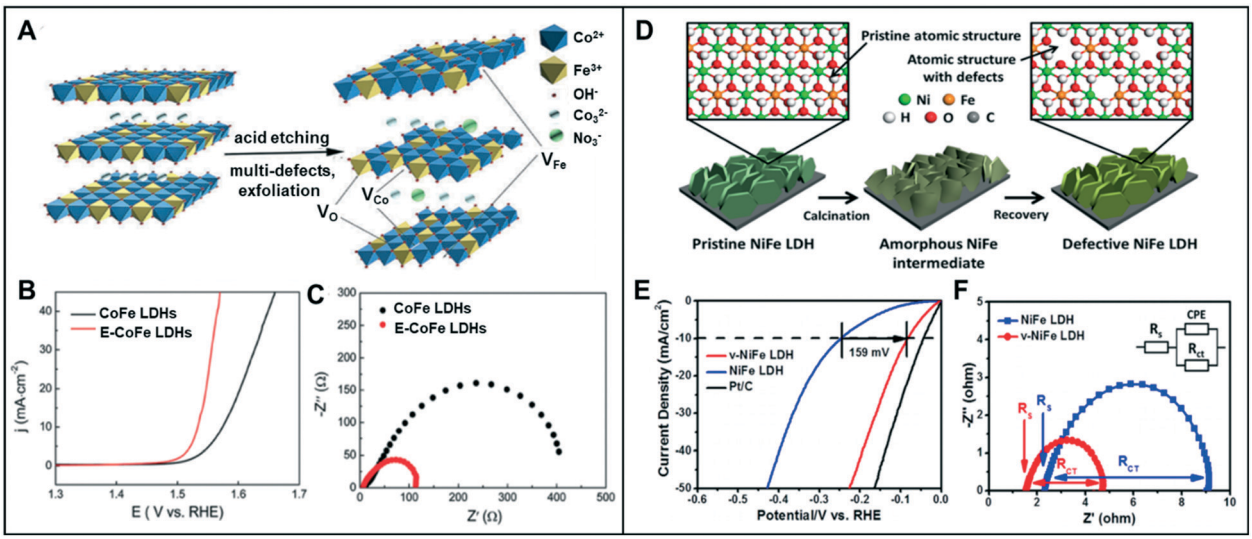

Fig. 7 (A) Schematic illustration of E-CoFe LDHs after HNO_3 etching. (B) OER performance of CoFe LDHs and E-CoFe LDHs in 1.0 M KOH. (C) Nyquist plots at an overpotential of 270 mV. Reproduced with permission from ref. 40. Copyright 2017 Royal Society of Chemistry. (D) Schematic illustration of defective NiFe LDH. (E) HER performance of v-NiFe LDH at a neutral pH. (F) Nyquist plots of pristine NiFe LDH and v-NiFe LDH nanosheets in 1.0 M PBS electrolyte. Reproduced with permission from ref. 42. Copyright 2019 American Chemical Society.

Table 1 Summary of vacancy-engineered electrocatalysts for the OER and HER

Catalyst	Vacancy type	Application	Electrolyte	Overpotential [mV@10 mA cm^{-2}]	Tafel slope [mV dec^{-1}]	Ref.
$SrCo_{0.9}Ir_{0.1}O_{3-\delta}$	Anion vacancy	OER	0.1 M $HClO_4$	250 mV@1 mA cm^{-2}	—	11
$IrNiO_x$	Anion vacancy	OER	0.05 M H_2SO_4	280 mV@0.2 mA g_{Ir}^{-1}	—	21
$NiCo_2O_4$ nanosheets	Anion vacancy	OER	1 M KOH	320 mV	30	28
Reduced NiFe	Anion vacancy	OER	1 M KOH	270 mV	40	31
CoO nanorods	Anion vacancy	OER	1 M KOH	330 mV	44	32
Reduced Co_3O_4 NWs	Anion vacancy	OER	1 M KOH	420 mV@13.1 mA cm^{-2}	72	26
Fe_1Co_1-ONS	Anion vacancy	OER	0.1 M KOH	308 mV	36.8	60
CoO_X(−4 h) nanoplates	Anion vacancy	OER	1 M KOH	306 mV	67	61
Plasma-engraved Co_3O_4 nanosheets	Anion vacancy	OER	0.1 M KOH	300 mV	68	62
YCRO-0.25	Anion vacancy	OER	0.5 M H_2SO_4	275 mV	40.3	63
Amorphous $MoS_{1.7}$	Anion vacancy	HER	0.5 M H_2SO_4	143 mV	39.5	33
MoS_2 basal plane	Anion vacancy	HER	0.5 M H_2SO_4	170 mV	60	9
NiO NRs-m-O_v	Anion vacancy	HER	1 M KOH	110 mV	100	1
Mesoporous MoO_{3-x}	Anion vacancy	HER	0.1 M KOH	138 mV	56	15
$MoS_{2-x}N_y$/rGO	Anion vacancy	HER	0.5 M H_2SO_4	217 mV	48	64
NiFe-V_M-O	Cation vacancy	OER	1 M NaOH	371 mV	28	22
$Co_{3-x}O_4$	Cation vacancy	OER	1 M KOH	268 mV	38.2	3
$CoSe_2$ nanosheets	Cation vacancy	OER	0.1 M KOH	320 mV	44	36
NiFe LDHs-V_{Ni} nanosheets	Cation vacancy	OER	1 M KOH	229 mV	62.9	65
SnCoFe-Ar	Cation vacancy	OER	1 M KOH	300 mV	42.3	66
FeP	Cation vacancy	HER	1 M KOH	108 mV	62	37
FeP	Cation vacancy	HER	0.5 M H_2SO_4	65 mV	49	37
PtPdRuTe AS	Cation vacancy	HER	1 M KOH	22 mV	22	39
Pt/np-$Co_{0.85}Se$	Cation vacancy	HER	1 M PBS	55 mV	35	67
$NiAl_\delta P$	Cation vacancy	HER	0.5 M H_2SO_4	35 mV	38	59
		OER	0.5 M H_2SO_4	256 mV	76	59
δ-FeOOH NSs/NF	Cation vacancy	HER	1 M KOH	108 mV	68	43
		OER	1 M KOH	265 mV	36	43
CoFe LDHs-Ar nanosheets	Multi vacancy	OER	1 M KOH	266 mV	37.85	41
E-CoFe LDHs	Multi vacancy	OER	1 M KOH	300 mV	41	40
NiFe-LDH nanosheets	Multi vacancy	OER	1 M KOH	254 mV	32	27
H_2O-Plasma exfoliated CoFe LDH	Multi vacancy	OER	1 M KOH	290 mV	36	68
NiFe LDHs	Multi vacancy	HER	1 M PBS	87 mV	46.3	42

effort to the controlled formation of multi-vacancies in catalytic materials.

For practical applications of the electrocatalysts, their stability, the intrinsic property dependent on the material phases, should be attained.[43] Vacancy engineering of electrocatalysts might provide solutions to the catalyst stability issues *via* optimized adsorption energy of intermediates and improved charge transfer in the catalyst structure. Some vacancy engineered catalysts with the high concentration of oxygen vacant sites have shown a superior stability toward OER, because the oxygen-vacant sites can form direct O–O bonds in the OER process, not necessitating significant reorganization of atoms within the catalysts.[29] Vacancy of other anions such as sulfur anions can also boost the catalyst stability; porous nanosheets of Co_3S_4 with abundant sulfur vacancies showed excellent stability toward the HER even at the high negative potentials.[44] Catalysts with sulfur vacancies, having more electrons, showed lower adsorption energy of H_2O, compared to other catalysts with no vacancy, accelerating electron/mass transfer and thus enhancing the stability.

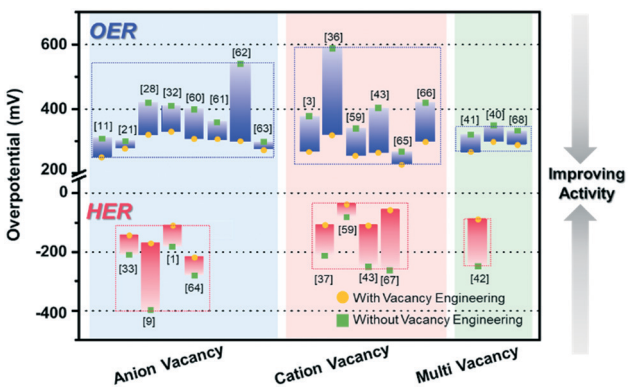

Fig. 8 Trend of the performance of recent vacancy-engineered electrocatalysts.

However, excessive vacancies in the catalysts could also induce adverse effects on structural stability and electronic conductivity.[45,46] Also, the issues for structural degradation and dissolution through vacant sites are far from being resolved. Therefore, the establishment of relationships between the catalytic stability and the number and nature of vacancies of the catalysts remains an important task in accomplishing the catalyst stability toward water splitting.

4. Future perspectives

The rapid growth of interest in engineering vacancy-rich electrocatalysts is a response to the increasing demand for highly efficient electrocatalysts. In this review, we aimed at providing an overview of the recent studies on vacancy-engineered catalysts for electrochemical HER and OER, regardless of metal types. These engineering vacancies in electrocatalysts could lead to the exposure of active sites through CUSs, optimization of adsorption energy for intermediates, and improvement of electrical conductivity. Based on these features from vacancy-engineered electrocatalysts, we could categorize the types of vacancies into anion, cation, and multi-vacancies. Despite the significant achievements in vacancy engineering toward water splitting in this review, the synthetic methodologies for the controlled formation of different vacancy types are severely underdeveloped. Therefore, continuous efforts on understanding the relationship between vacancy formation and catalytic performance are necessary to rationally design vacancy-optimized electrocatalysts. Some representative future perspectives are schematically shown in Fig. 9.

4.1. Beyond anion vacancy engineering: importance of cation and multi-vacancy

The most remarkable challenges for vacancy engineering are the limited methods to induce cation vacancies because the formation energy of metal/cation vacancy is quite higher than that of anion vacancy.[47] However, as discussed in Table 1 and Fig. 8, the cation or metal vacancy-engineered catalysts could largely improve the catalytic activity for both OER and HER. This is because the excess electrons can facilitate the modulation of the electronic structure on the catalyst surface. Therefore, additional research to create metal/cation vacancies to generate OER and HER active sites on the atomic level should be conducted. Moreover, several studies have proven that multi (anion and cation) vacancies within one material can have synergistic effects to accelerate the water electrolysis process. In this context, the engineering of multi-vacancies with various catalytic materials is direly required for enhancing electrochemical water-splitting reactions.

4.2. Development of a novel vacancy from noble metal-based electrocatalysts

The development of noble metal vacancies is also necessary. In acidic OER/HER, noble metals such as Ir, Ru, and Pt have been greatly utilized because of their excellent intrinsic performances for electrolysis. Although the dissolution rates of noble metals during electrochemical catalysis are lower than those of non-noble metals, a small amount of noble metals can still be traced in the electrolyzers.[11,48] Although such dissolution can initiate defects in the electrocatalysts with noble metal vacancies, these vacancies could not be finely controlled. The formation of well-defined noble metal vacancies can lead to the great modification of metal coordination, which can provide additional active sites and improve the electrocatalytic performance of water splitting in both acidic and alkaline media using a relatively small amount of noble metals. Thus, further studies on noble metal-based vacancies are required.

4.3. Constructing the stability of vacancy-engineered electrocatalysts

Very few studies have been conducted to understand the relationship between the formation of vacancies and catalyst stability. Because the vacancies in the structures can lead to geometrical and electronic distortions,[49] a weaker bonding of the lattice in defective structures compared to that in crystalline ones might be induced, which would lead to the formation of

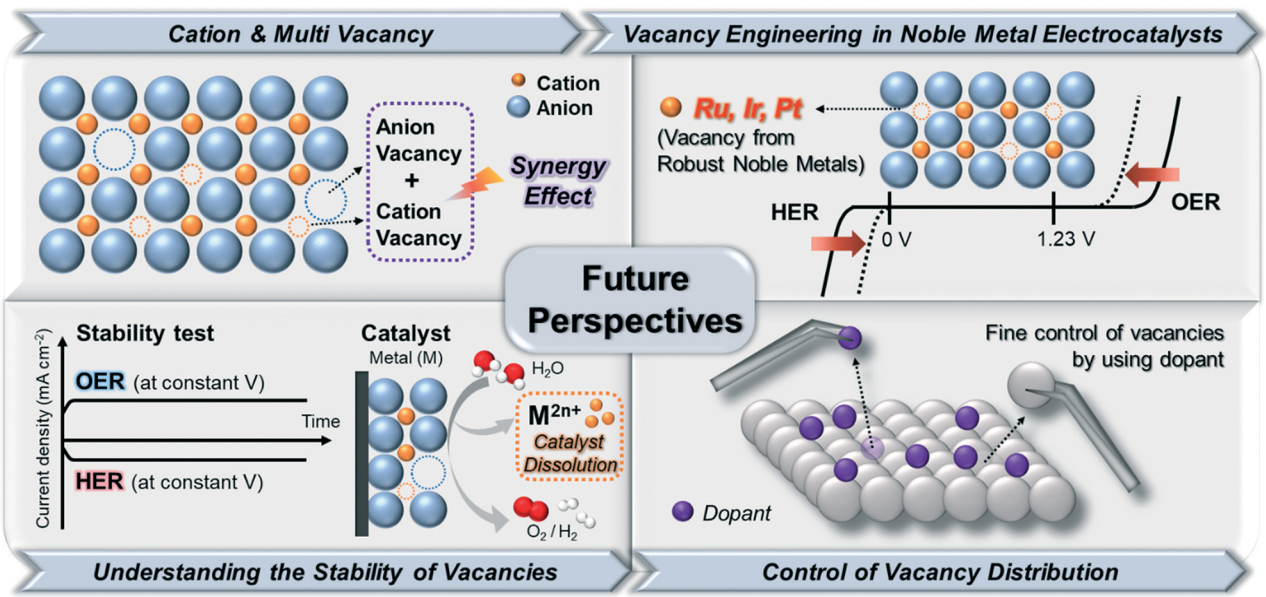

Fig. 9 Illustration of future perspectives for enhancing the performance of electrocatalytic water splitting *via* vacancy engineering.

metastable structures and accelerate the degradation of catalyst structures in the electrocatalysts.[48] To prevent the degradation of electrocatalysts, an understanding of the surrounding atoms adjacent to the vacant sites and their overall chemical environments is necessary to design highly robust electrocatalysts with numerous active sites. Although a few studies on the theoretical investigation of thermodynamic stability and vacancy formation has been reported,[50–52] experimental research demonstrating the relationship between an optimal vacancy formation and stability of electrocatalysts should also be conducted to verify the theory-based predictions.

4.4. Efforts on the elaborate control of the vacancy distribution

To aid the development of vacancy formation, advances in synthetic methods (both physical and chemical) to form and identify vacancies are greatly required. The energy to create vacancies can be provided by physical methods, such as plasma etching,[9] thermal treatment,[53] liquid exfoliation,[27,54] and electrochemical etching.[11,21] These physical methods used to create vacancies could be modulated by varying the processing time and energy input.[18] Meanwhile, the creation of vacancies can occur simultaneously with chemical reactions, such as chemical reduction,[55] hydrothermal synthesis,[56] and elemental doping.[57] Therefore, because it is difficult to predict and precisely control the vacancy distribution, elemental doping into existing materials might be an effective route to create atomically controlled vacancies.[58] Depending on the type of dopants with different ionic sizes, the positions and sizes of the formed vacancy sites could be deterministically controlled. For example, in perovskites (ABO_3, where A and B are cations, with A atoms larger than B atoms; X is an anion that bonds with both cations), small ions are exclusively doped on the B-site and oxygen vacancies are created for charge composition if the dopant has a relatively low valence.[57,58] This can also result in the partial oxidation or reduction of ions on the B sites or result in the appearance of B-site vacancies if the dopant has a high valence. Conversely, if large ions are substituted only on the A-site, A-site, B-site, or oxygen vacancies can be created, depending on the induced charge balance of the crystal structure. Therefore, the choice of doping element types can determine the different sizes and sites of vacancies, which can lead to the discovery of more active sites on the electrocatalysts. As with the case of perovskites, the atomically modulated vacancies *via* elemental doping might be applied to various types of crystal structures, such as hetero-interface structures. Nanostructures with hetero-interfaces can be promising platforms for providing a pathway through which dopants can easily move between different phases under relatively low energy, compared to nanostructures without interfaces. This might lead to the formation of numerous vacancies after leaching out the dopants. The position and number of vacancies might be conveniently controlled by modulating the diffusion zone width within the nanocrystals.[58]

Furthermore, even if the materials have the same crystal structure and geometry, the shape-controlled materials might have different properties when the vacancy is formed on the exposed surface. Shape-controlled materials that expose the different specific facets can have facet-specific vacancy types on the surface of the catalysts due to the differences in the coordination environments for different facet types. Investigation of catalysis on facet-specific vacancy might allow us to understand further structural details of the highly active vacancies toward water electrolysis.

5. Conclusion

In summary, vacancy engineering has been considered as an effective strategy for the development of highly efficient electrocatalysts for water electrolysis. The vacancy-controlled catalysts are endowed with useful properties such as exposure of low-coordination sites, optimized adsorption energies of intermediates, and enhanced electrical conductivity. In addition, the vacancy-engineered electrocatalysts show great potential toward the water-splitting reactions, namely OER and HER. However, synthetic approaches are quite underdeveloped toward position-controlled and quantity-controlled vacancy formation within the nanostructures. Therefore, the development of atomic-scale engineering for the precise tuning of vacancies and alteration of coordination environments for vacancies should be developed for further improvement of active and stable electrocatalysts. We hope that this review can motivate active developments of vacancy-engineered electrocatalysts for water electrolysis and other related energy applications.

Conflicts of interest

There are no conflicts to declare.

Acknowledgements

This study was supported by the National Research Foundation of Korea (NRF-2017R1A2B3005682, NRF2019R1A6A1A11044070), and the Hydrogen Energy Innovation Technology Development Program of the National Research Foundation of Korea (NRF) funded by the Korean Government (Ministry of Science and ICT(MSIT)) (No. NRF-2019M3E6A1064709).

References

1 T. Zhang, M.-Y. Wu, D.-Y. Yan, J. Mao, H. Liu, W.-B. Hu, X.-W. Du, T. Ling and S.-Z. Qiao, *Nano Energy*, 2018, **43**, 103–109.
2 Z. Chen, C. X. Kronawitter, Y.-W. Yeh, X. Yang, P. Zhao, N. Yao and B. E. Koel, *J. Mater. Chem. A*, 2017, **5**, 842–850.
3 R. Zhang, Y.-C. Zhang, L. Pan, G.-Q. Shen, N. Mahmood, Y.-H. Ma, Y. Shi, W. Jia, L. Wang, X. Zhang, W. Xu and J.-J. Zou, *ACS Catal.*, 2018, **8**, 3803–3811.
4 Y. Sun, S. Gao, F. Lei and Y. Xie, *Chem. Soc. Rev.*, 2015, **44**, 623–636.

5 S. H. Brodersen, U. Grønbjerg, B. Hvolbæk and J. Schiøtz, *J. Catal.*, 2011, **284**, 34–41.
6 Y. Sun, S. Gao, F. Lei, J. Liu, L. Liang and Y. Xie, *Chem. Sci.*, 2014, **5**, 3976–3982.
7 J. V. Lauritsen, J. Kibsgaard, S. Helveg, H. Topsøe, B. S. Clausen, E. Lægsgaard and F. Besenbacher, *Nat. Nanotechnol.*, 2007, **2**, 53–58.
8 T. F. Jaramillo, K. P. Jørgensen, J. Bonde, J. H. Nielsen, S. Horch and I. Chorkendorff, *Science*, 2007, **317**, 100.
9 H. Li, C. Tsai, A. L. Koh, L. Cai, A. W. Contryman, A. H. Fragapane, J. Zhao, H. S. Han, H. C. Manoharan, F. Abild-Pedersen, J. K. Nørskov and X. Zheng, *Nat. Mater.*, 2016, **15**, 48–53.
10 S. Jayabal, G. Saranya, J. Wu, Y. Liu, D. Geng and X. Meng, *J. Mater. Chem. A*, 2017, **5**, 24540–24563.
11 Y. Chen, H. Li, J. Wang, Y. Du, S. Xi, Y. Sun, M. Sherburne, J. W. Ager, A. C. Fisher and Z. J. Xu, *Nat. Commun.*, 2019, **10**, 572.
12 H. Jin, C. Guo, X. Liu, J. Liu, A. Vasileff, Y. Jiao, Y. Zheng and S.-Z. Qiao, *Chem. Rev.*, 2018, **118**, 6337–6408.
13 Q. Ding, B. Song, P. Xu and S. Jin, *Chem*, 2016, **1**, 699–726.
14 Y. Liu, C. Xiao, P. Huang, M. Cheng and Y. Xie, *Chem*, 2018, **4**, 1263–1283.
15 Z. Luo, R. Miao, T. D. Huan, I. M. Mosa, A. S. Poyraz, W. Zhong, J. E. Cloud, D. A. Kriz, S. Thanneeru, J. He, Y. Zhang, R. Ramprasad and S. L. Suib, *Adv. Energy Mater.*, 2016, **6**, 1600528.
16 Y.-W. Cheng, J.-H. Dai, Y.-M. Zhang and Y. Song, *J. Mater. Chem. A*, 2018, **6**, 20956–20965.
17 T. Reier, H. N. Nong, D. Teschner, R. Schlögl and P. Strasser, *Adv. Energy Mater.*, 2017, **7**, 1601275.
18 M.-Q. Yang, J. Wang, H. Wu and G. W. Ho, *Small*, 2018, **14**, 1703323.
19 K. S. Exner and H. Over, *ACS Catal.*, 2019, **9**, 6755–6765.
20 V. Pfeifer, T. E. Jones, S. Wrabetz, C. Massué, J. J. Velasco Vélez, R. Arrigo, M. Scherzer, S. Piccinin, M. Hävecker, A. Knop-Gericke and R. Schlögl, *Chem. Sci.*, 2016, **7**, 6791–6795.
21 H. N. Nong, T. Reier, H.-S. Oh, M. Gliech, P. Paciok, T. H. T. Vu, D. Teschner, M. Heggen, V. Petkov, R. Schlögl, T. Jones and P. Strasser, *Nat. Catal.*, 2018, **1**, 841–851.
22 H. J. Lee, S. Back, J. H. Lee, S. H. Choi, Y. Jung and J. W. Choi, *ACS Catal.*, 2019, **9**, 7099–7108.
23 H.-S. Kim, J. B. Cook, H. Lin, J. S. Ko, S. H. Tolbert, V. Ozolins and B. Dunn, *Nat. Mater.*, 2017, **16**, 454–460.
24 M. Dieterle, G. Weinberg and G. Mestl, *Phys. Chem. Chem. Phys.*, 2002, **4**, 812–821.
25 G. Wang, Y. Ling and Y. Li, *Nanoscale*, 2012, **4**, 6682–6691.
26 Y. Wang, T. Zhou, K. Jiang, P. Da, Z. Peng, J. Tang, B. Kong, W.-B. Cai, Z. Yang and G. Zheng, *Adv. Energy Mater.*, 2014, **4**, 1400696.
27 Y. Zhao, X. Zhang, X. Jia, G. I. N. Waterhouse, R. Shi, X. Zhang, F. Zhan, Y. Tao, L.-Z. Wu, C.-H. Tung, D. O'Hare and T. Zhang, *Adv. Energy Mater.*, 2018, **8**, 1703585.
28 J. Bao, X. Zhang, B. Fan, J. Zhang, M. Zhou, W. Yang, X. Hu, H. Wang, B. Pan and Y. Xie, *Angew. Chem., Int. Ed.*, 2015, **54**, 7399–7404.
29 S. Hirai, K. Morita, K. Yasuoka, T. Shibuya, Y. Tojo, Y. Kamihara, A. Miura, H. Suzuki, T. Ohno, T. Matsuda and S. Yagi, *J. Mater. Chem. A*, 2018, **6**, 15102–15109.
30 L. Han, S. Dong and E. Wang, *Adv. Mater.*, 2016, **28**, 9266–9291.
31 M. Asnavandi, Y. Yin, Y. Li, C. Sun and C. Zhao, *ACS Energy Lett.*, 2018, **3**, 1515–1520.
32 T. Ling, D.-Y. Yan, Y. Jiao, H. Wang, Y. Zheng, X. Zheng, J. Mao, X.-W. Du, Z. Hu, M. Jaroniec and S.-Z. Qiao, *Nat. Commun.*, 2016, **7**, 12876.
33 A.-Y. Lu, X. Yang, C.-C. Tseng, S. Min, S.-H. Lin, C.-L. Hsu, H. Li, H. Idriss, J.-L. Kuo, K.-W. Huang and L.-J. Li, *Small*, 2016, **12**, 5530–5537.
34 B. T. Sneed, A. P. Young and C.-K. Tsung, *Nanoscale*, 2015, **7**, 12248–12265.
35 J. Suntivich, K. J. May, H. A. Gasteiger, J. B. Goodenough and Y. Shao-Horn, *Science*, 2011, **334**, 1383.
36 Y. Liu, H. Cheng, M. Lyu, S. Fan, Q. Liu, W. Zhang, Y. Zhi, C. Wang, C. Xiao, S. Wei, B. Ye and Y. Xie, *J. Am. Chem. Soc.*, 2014, **136**, 15670–15675.
37 W. L. Kwong, E. Gracia-Espino, C. C. Lee, R. Sandström, T. Wågberg and J. Messinger, *ChemSusChem*, 2017, **10**, 4544–4551.
38 W. L. Kwong, C. C. Lee and J. Messinger, *J. Phys. Chem. C*, 2017, **121**, 284–292.
39 S. Liu, X. Mu, W. Li, M. Lv, B. Chen, C. Chen and S. Mu, *Nano Energy*, 2019, **61**, 346–351.
40 P. Zhou, Y. Wang, C. Xie, C. Chen, H. Liu, R. Chen, J. Huo and S. Wang, *Chem. Commun.*, 2017, **53**, 11778–11781.
41 Y. Wang, Y. Zhang, Z. Liu, C. Xie, S. Feng, D. Liu, M. Shao and S. Wang, *Angew. Chem., Int. Ed.*, 2017, **56**, 5867–5871.
42 Z. Yuan, S.-M. Bak, P. Li, Y. Jia, L. Zheng, Y. Zhou, L. Bai, E. Hu, X.-Q. Yang, Z. Cai, Y. Sun and X. Sun, *ACS Energy Lett.*, 2019, **4**, 1412–1418.
43 J. Kim, M. Jun, S. Choi, J. Jo and K. Lee, *Nanoscale*, 2019, **11**, 20392–20410.
44 C. Zhang, Y. Shi, Y. Yu, Y. Du and B. Zhang, *ACS Catal.*, 2018, **8**, 8077–8083.
45 J. Du, T. Zhang, F. Cheng, W. Chu, Z. Wu and J. Chen, *Inorg. Chem.*, 2014, **53**, 9106–9114.
46 Y. Guo, Y. Tong, P. Chen, K. Xu, J. Zhao, Y. Lin, W. Chu, Z. Peng, C. Wu and Y. Xie, *Adv. Mater.*, 2015, **27**, 5989–5994.
47 B. Liu, Y. Wang, H.-Q. Peng, R. Yang, Z. Jiang, X. Zhou, C.-S. Lee, H. Zhao and W. Zhang, *Adv. Mater.*, 2018, **30**, 1803144.
48 S. Geiger, O. Kasian, M. Ledendecker, E. Pizzutilo, A. M. Mingers, W. T. Fu, O. Diaz-Morales, Z. Li, T. Oellers, L. Fruchter, A. Ludwig, K. J. J. Mayrhofer, M. T. M. Koper and S. Cherevko, *Nat. Catal.*, 2018, **1**, 508–515.
49 A. A. Emery and C. Wolverton, *Sci. Data*, 2017, **4**, 170153.
50 B. Liu, D. S. Aidhy, Y. Zhang and W. J. Weber, *Phys. Chem. Chem. Phys.*, 2014, **16**, 25461–25467.
51 S. M. Alay-e-Abbas, S. Nazir, N. A. Noor, N. Amin and A. Shaukat, *J. Phys. Chem. C*, 2014, **118**, 19625–19634.
52 D. Le, T. B. Rawal and T. S. Rahman, *J. Phys. Chem. C*, 2014, **118**, 5346–5351.
53 L. Li, T. Zhang, J. Yan, X. Cai and S. Liu, *Small*, 2017, **13**, 1700441.

54 Y. Xu, L. Wang, X. Liu, S. Zhang, C. Liu, D. Yan, Y. Zeng, Y. Pei, Y. Liu and S. Luo, *J. Mater. Chem. A*, 2016, **4**, 16524–16530.
55 C. Zhu, S. Fu, D. Du and Y. Lin, *Chem. – Eur. J.*, 2016, **22**, 4000–4007.
56 Y. Zhao, C. Chang, F. Teng, Y. Zhao, G. Chen, R. Shi, G. I. N. Waterhouse, W. Huang and T. Zhang, *Adv. Energy Mater.*, 2017, **7**, 1700005.
57 Y. Wang, J. Piao, G. Xing, Y. Lu, Z. Ao, N. Bao, J. Ding, S. Li and J. Yi, *J. Mater. Chem. C*, 2015, **3**, 11953–11958.
58 G. Li, G. R. Blake and T. T. M. Palstra, *Chem. Soc. Rev.*, 2017, **46**, 1693–1706.
59 W. Cheng, H. Zhang, X. Zhao, H. Su, F. Tang, J. Tian and Q. Liu, *J. Mater. Chem. A*, 2018, **6**, 9420–9427.
60 L. Zhuang, L. Ge, Y. Yang, M. Li, Y. Jia, X. Yao and Z. Zhu, *Adv. Mater.*, 2017, **29**, 1606793.
61 W. Xu, F. Lyu, Y. Bai, A. Gao, J. Feng, Z. Cai and Y. Yin, *Nano Energy*, 2018, **43**, 110–116.
62 L. Xu, Q. Jiang, Z. Xiao, X. Li, J. Huo, S. Wang and L. Dai, *Angew. Chem., Int. Ed.*, 2016, **55**, 5277–5281.
63 Q. Feng, Z. Zhao, X.-Z. Yuan, H. Li and H. Wang, *Appl. Catal., B*, 2020, **260**, 118176.
64 Z. Luo, Y. Wang, X. Wang, Z. Jin, Z. Wu, J. Ge, C. Liu and W. Xing, *ACS Appl. Mater. Interfaces*, 2019, **11**, 39782–39788.
65 Y. Wang, M. Qiao, Y. Li and S. Wang, *Small*, 2018, **14**, 1800136.
66 D. Chen, M. Qiao, Y.-R. Lu, L. Hao, D. Liu, C.-L. Dong, Y. Li and S. Wang, *Angew. Chem., Int. Ed.*, 2018, **57**, 8691–8696.
67 K. Jiang, B. Liu, M. Luo, S. Ning, M. Peng, Y. Zhao, Y.-R. Lu, T.-S. Chan, F. M. F. de Groot and Y. Tan, *Nat. Commun.*, 2019, **10**, 1743.
68 R. Liu, Y. Wang, D. Liu, Y. Zou and S. Wang, *Adv. Mater.*, 2017, **29**, 1701546.